Robust Optical Mode Conversion in Waveguides by Triplet Supercell

Wange Song[1,2] Shengjie Wu,[1,2] Yuxin Chen,[1,2] Chen Chen[1,2] Shenglun Gao[1,2] Chunyu Huang,[1]
Kai Qiu,[1] Shining Zhu,[1,2] and Tao Li[1,2,*]

[1]*National Laboratory of Solid State Microstructures, Key Laboratory of Intelligent Optical Sensing and Manipulations, Jiangsu Key Laboratory of Artificial Functional Materials, College of Engineering and Applied Sciences, Nanjing University, Nanjing, 210093, China*
[2]*Collaborative Innovation Center of Advanced Microstructures, Nanjing, 210093, China*

On-chip mode conversion is beneficial in photonic integrations and enables many functionalities for optical signal processing, however, it is still challenging to achieve a robust solution with broadband working wavelengths. Here, by exploring an interesting coupling effect between triplet and singlet waveguides, we propose and realize a robust mode conversion based on an undistributed breathing mode in the waveguide triplet supercell. It is well demonstrated with high efficiency and robustness in the silicon waveguide platform, which shows further extensions to higher-order mode conversions by connecting more elements together. Our approach makes good use of the undisturbed breathing modes in a three-level system for robust mode conversions, which is proved to be an effective means and promises further functional elements in photonic integrations.

I. INTRODUCTION

Integrated photonics provides a promising platform for information processing and high-speed communication, though there are still key problems to be solved at the device level that prevent reliable, massive integration, including device miniaturization, operation bandwidth, device robustness, and minimizing the insertion loss [1–4]. Early work has demonstrated some on-chip mode converters by a mode interferometer with a complicated structure [5,6]. In these designs, the mode conversions rely on the phase control in waveguides by light propagations that are very sensitive to the waveguide parameters. Recently, some mode converters have been proposed by inversed design methods or by using metasurfaces with very small footprints [7–15], while the performances are still vulnerable to structural fluctuations. In addition, they inevitably increase the insertion losses and complicate the fabrication, which does not favor efficient photonic integration. Interestingly, increasing attention has been given to realizing asymmetric mode conversion by adiabatically encircling the exceptional points (EPs), but still at the cost of inefficiency and large footprints [16–21]. In fact, the concept of supersymmetry was also proposed to realize the mode conversion in Hermitian and static systems [22,23]. Nevertheless, this mode conversion is still vulnerable to structure variations due to the stringent mode-matching conditions. As can be seen, it remains a big challenge to

achieve high-performance on-chip mode conversion with structure tolerance, as well as low insertion loss in the broadband.

Here, we explore the coupling effect between a triplet supercell and singlet waveguides, which enables a robust mode conversion with high efficiency. In the triplet waveguide supercell, there is a breathing mode with a zero mode constant and two split translation modes, where the breathing zero mode can be coupled to a singlet waveguide aside. Specifically, the input light from the singlet waveguide will be efficiently transferred to the triplet supercell with an antisymmetric breathing-mode output. Therefore, a compact mode converter is successfully implemented in silicon waveguide experiments at telecommunication wavelength. Moreover, its performance is found to be very robust to the structure variations and working wavelengths, which can be attributed to the breathing mode in the triplet supercell with an undisturbed mode constant.

II. BREATHING MODE IN WAVEGUIDE TRIPLET

Figure 1(a) schematically shows the triplet waveguide supercell, whose eigenmodes can be described by a three-level Hamiltonian, where β_0 is the mode constant of a single isolated waveguide, c_1 and c_2 are the coupling coefficients. The eigenmode constants and distributions of the waveguide triplet can be calculated by coupled-mode theory (CMT) [24,25] (see Appendix A for details). Figure 1(b) shows three-level eigenmodes with their mode profiles and there is a special mode pinned
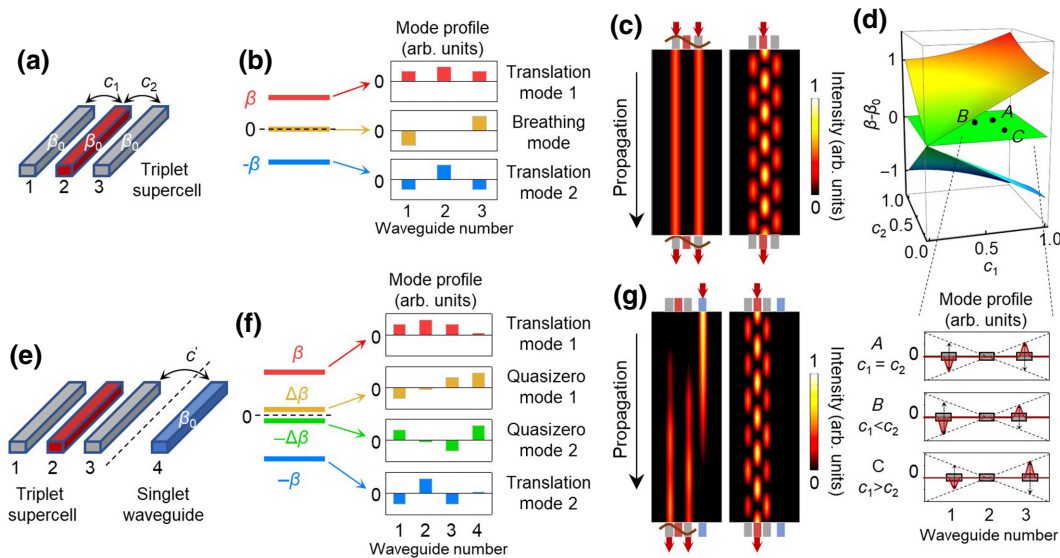
*taoli@nju.edu.cn

FIG. 1. (a) Schematics of the triplet waveguide supercell. (b) Mode-constant levels and corresponding mode profiles of triplet supercell, here $c_1 = c_2$. (c) CMT-calculated electric-field-intensity evolution with breathing-mode input (left panel) and waveguide-2 inputs (right panel). (d) Mode constants as functions of c_1 and c_2, where the breathing modes with undistributed zero mode constant always exist (green plane). Bottom panel: breathing-mode profiles under different c_1 and c_2 conditions, the amplitude on central waveguide remains zero. (e) Schematics of the coupling of the singlet waveguide to the triplet supercell. (f) Mode-constant levels and corresponding mode profiles. (g) CMT-calculated electric-field-intensity evolution with waveguide-4 and -2 inputs.

at zero (unchanged β_0) and two split modes. The special mode has an antisymmetric mode profile at two side waveguides while having no field at the central one, which is referred to as the *breathing mode* [26,27]. In contrast, the two split modes have the mode profiles of maximum field at the center with in phase or out of phase on two sides, which are termed "translation modes" here. Thus, the breathing mode can only be excited by antiphased input from two side waveguides [Fig. 1(c), left panel]. Instead, the center waveguide input can excite two translation modes simultaneously, resulting in a beating effect due to the different mode constants [Fig. 1(c), right panel]. Notably, the breathing mode can preserve its mode properties even as the two coupling coefficients, c_1 and c_2, vary, i.e., it always pins at zero level with zero field at the central waveguide, while the two side waveguides always have an antiphased profile [see Fig. 1(d)].

Since the breathing mode of the triplet supercell has a stable zero mode constant even with large parameter variations, it is quite possible to be efficiently coupled to a relatively "isolated" waveguide aside. Thus, we place a singlet waveguide (blue one, waveguide 4) beside the triplet supercell with coupling coefficient c' ($c' < c_i$, $i = 1,2$), as shown in Fig. 1(e). This case resembles a four-level system, i.e., coupling a three-level system of a triplet supercell to a one-level system of a singlet waveguide. This coupling will split the original breathing modes away from exact zero, and form two coupled *quasizero modes* (QZMs). They exhibit hybrid properties that are mainly located at

waveguide 4 and waveguides 1, 3 of the triplet supercell [almost none at waveguide 2, see Fig. 1(f)]. In contrast, the two splitting translation modes are almost unchanged due to huge mismatch for mode coupling to the singlet waveguide 4. Therefore, the input light from waveguide 4 will reasonably excite two QZMs due to large mode distribution at the waveguide, which then transfers the energy to the triplet supercell with an antiphased field distribution at the output, as shown in Fig. 1(g) (left panel) (see Appendix B for experimental confirmation). Otherwise, when we input light from waveguide 2 (center waveguide of the triplet supercell), two translation modes will be excited simultaneously with a beating effect, and localized at the triplet supercell [see Fig. 1(g), right panel].

III. ROBUST MODE CONVERSION

Interestingly, these mode properties enable the realization of mode conversion. Here, we would like to show the implementation in the silicon waveguide platform. The device is designed in silicon waveguides 220 nm thick and 400 nm wide, allowing a fundamental symmetric TE_{00} mode with a wave vector of $2.16k_0$ at 1550 nm wavelength (k_0 is wave number in the vacuum). The four waveguides are arranged with spaces of $d' = 200$ nm and $d_1 = d_2 = 120$ nm corresponding to $c' = 0.020k_0$ and $c_1 = c_2 = 0.037k_0$, respectively, and the length of waveguides is 29.5 μm. Furthermore, we connect waveguide 1 and 3 of the triplet waveguides to form a two-mode
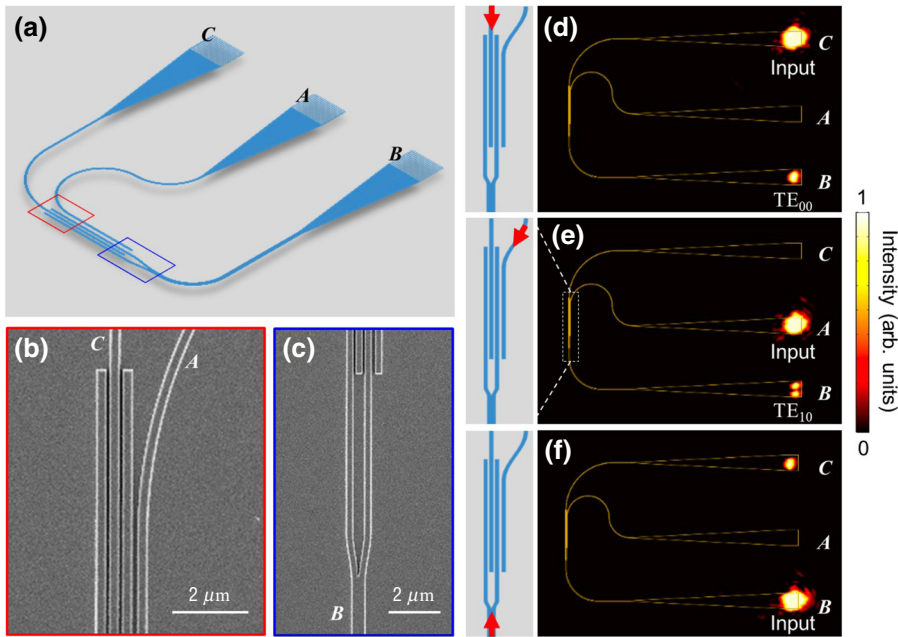
FIG. 2. (a)–(c) Schematics and enlarged SEM pictures of the fabricated samples. (d)–(f) Experimentally recorded optical propagation from input to output through the device.

Si waveguide (with a width of 800 nm). Waveguide 4, two-mode waveguide, and waveguide 2 are extended out and connected to grating couplers through tapered waveguides, marked by ports A, B, and C, respectively, as the schematics and SEM images shown in Figs. 2(a)–2(c). In experiments, a focused laser (1550 nm) is input at the three ports, respectively, and the corresponding light-transport results are revealed from captured light spots from these ports, as shown in Figs. 2(d)–2(f) (see Appendix C for sample fabrication and measurement). It can be seen that the light input from port A is routed to port B with two bright spots, which expectedly corresponds to a mode conversion of input TE_{00} to the high-order TE_{10} [Fig. 2(e)]. If we switch the input to port C, there is only one bright spot, indicating the characteristics of the fundamental TE_{00} mode [Fig. 2(d)]. Thus, we could realize the mode switching by changing the input ports. In addition, if we input the light from port B, then the light will be only routed to port C [see Fig. 2(f)], and no light comes out from port A (see Appendix D for details).

Significantly, the mode conversions are found to be very robust to the structure variations. Here, we intentionally introduce random position variations of waveguides corresponding to the variations in coupling coefficient as $c_i[1 + (\alpha/2)\xi_i]$ between the ith and $(i+1)$th waveguides, where ξ_i is random numbers in the interval $[-1,1]$, α is the variation amplitude. In experiments, we fabricate the samples with only ports A and B with different waveguide position variations (the maximum variation $\Delta_{max} = 48$ nm corresponds to $\alpha = 0.64$) to systematically investigate the robustness of mode conversion from port A to B. It is found that the mode-conversion process is still valid even for large structure discrepancies [Fig. 3(a), see Appendix E

for more details]. In fact, this tolerance to the structure variations also indicates the insensitivity to the working wavelengths. Further experiments are performed with respect to different wavelengths and the results are shown in Fig. 3(b). It well confirms the robustness of mode-conversion performance as long as the relation between the triplet supercell and singlet waveguide is maintained, regardless of wavelength changes. In Fig. 3(b), the inconspicuous of two spot lobes as the wavelength increases would account for the multimode condition gradually diminishing. It is worthwhile to mention that the straight waveguide design makes the device quite efficient. By comparing the intensity distributions of port B to that of a referenced single straight waveguide [see Fig. 3(c)], we do not observe a significant difference in transmitted optical power between these two in experiments and obtain low insertion-loss data of approximately 0.32 dB for the device (see more details in Appendix F).

As mentioned, the breathing mode has an undisturbed zero mode constant and zero field at the center waveguide [Fig. 1(d)], which rightly gives rise to the robust mode-conversion behaviors. Here, we further check these two robust signatures in random variations in waveguide positions by massive calculations, as the mode results plotted in Fig. 3(d) (1000 samples are checked). It is found that the breathing modes are always pinned at zero level, and the mode profile maintains zero weight at waveguide 2 for all levels of variations. Thus, the modes' input from waveguide 4 can always couple to the triplet waveguide supercell with antisymmetric breathing-mode output. The calculated field evolutions in samples with different variations ($\alpha = 0.5, 1$) intuitively show this process [Fig. 3(e), see more results in Appendix E]. Note that QZMs are very
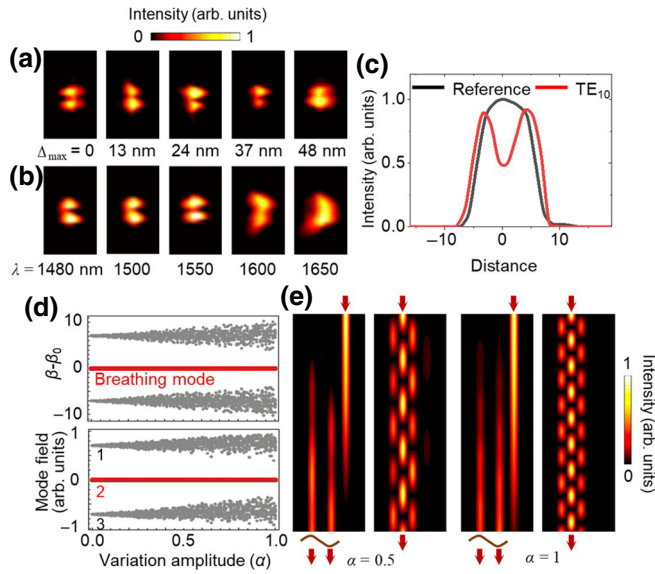
FIG. 3. Experimentally captured light intensities of port *B* for samples with structure variations (a) and different wavelengths (b). (c) Extracted intensity distributions of port *B* and referenced single waveguide output. (d) Mode constants (top) and field of breathing mode (bottom) in the presence of position variations for the triplet supercell, 1000 samples are checked and presented here. (e) Light-propagation patterns with structure variations ($\alpha = 0.5, 1$).

stable and the π-phase difference at the output waveguides 1 and 3 is always perfectly preserved [see Fig. 7(g)], which rightly contributes to a robust mode conversion as these two waveguides are connected to a multimode waveguide, and have been well verified in our experiments.

Furthermore, this design has good extendibility for higher-order mode conversions. By using this functional element as the building block, a high-order TE_{i0} mode
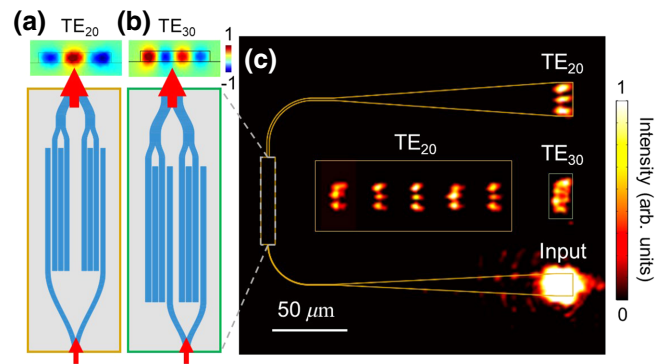

FIG. 4. (a), (b) Schematics and simulation results of generating high-order modes by using this functional element as the building block. (c) Corresponding experimental results, where three and four lobes are clearly observed from the output ports indicating the generation of the TE_{20} and TE_{30} mode. The insert (orange box) shows the generated TE_{20} mode by measuring multiple samples.

can be produced. For example, we demonstrate the TE_{20} and TE_{30} modes that are generated by combining two elements as schematically shown in Figs. 4(a) and 4(b). They are well verified in our Si waveguide experiments [see Fig. 4(c)], where three and four lobes are clearly observed from the output ports indicating the generation of the TE_{20} and TE_{30} modes. In the case of TE_{20}-mode generation, we test multiple samples and find they all have good mode profiles with clear triplet lobes, confirming the robust mode conversion.

IV. CONCLUSION

In summary, we report a robust optical mode conversion by coupled waveguides without additional nanostructures or adiabatic designs. In fact, the triplet waveguide supercell design is quite simple only with straight waveguides. This is distinct from more complicated setups with nanostructures for phase matching [12–15] and non-Hermitian systems with dynamically encircling the EP [16–21], where more losses and fabrication challenges are inevitable. More interestingly, the proposed waveguide supercell hosts a robust breathing mode that plays a key role in realizing such a mode conversion. In this regard, our approach provides a simple and stable scheme for flexible mode manipulation, which holds great promise for high-efficient robust on-chip photonic integrations.

ACKNOWLEDGMENTS

APPENDIX A: THEORETICAL CALCULATION

Following the CMT in the tight-binding approximation [24,25], the optical-field propagation within the coupled waveguides can be described by

$$-i\frac{\partial}{\partial z}\varphi_j = \beta_j \varphi_j + c_{j,j-1}\varphi_{j-1} + c_{j,j+1}\varphi_{j+1}, \quad \text{(A1)}$$

where φ_j denotes the optical field in the jth waveguide and β_j is the corresponding onsite propagation constants. $c_{j,j+1}$ is the coupling coefficient of the nearest neighbors. z is the propagation direction. Note that the CMT equation is mathematically equivalent to the time-dependent Schrödinger equation, therefore, the evolution of the light field in the waveguide array simulates the time-dependent wave function in the Schrödinger equation with propagation distance z being the effective time and propagation constant β being effective energy. From Eq. (A1),
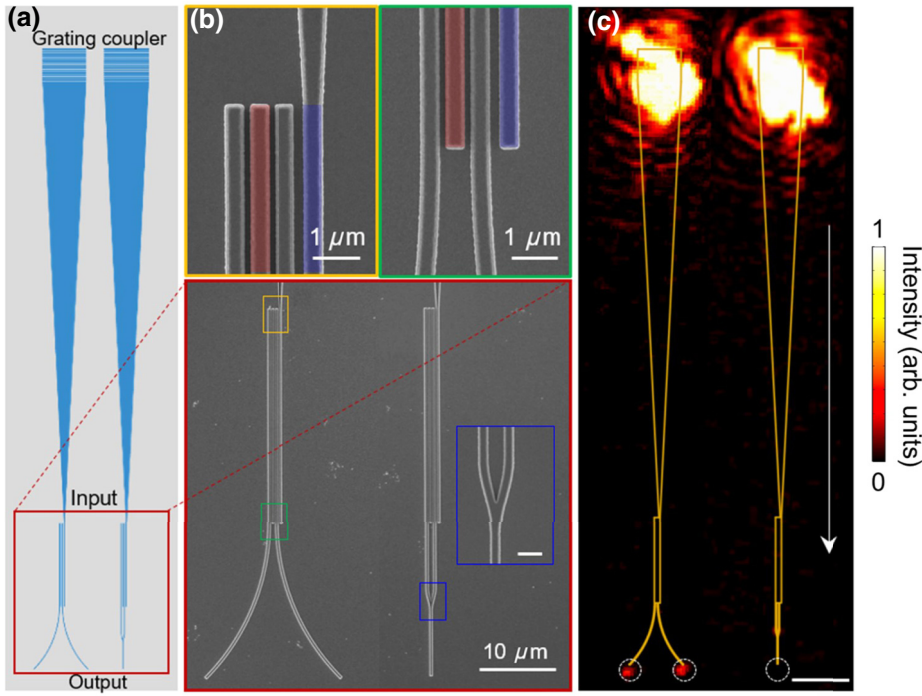
FIG. 5. (a), (b) Schematics and SEM pictures of the phase inverter device. One sample with two extended waveguides is designed to examine the intensities, while the other sample with one combined waveguide is to examine the phase difference. (c) Experimental results. Scale bar $= 20$ μm.

the Hamiltonian of the waveguide array can be written in the matrix form:

$$H = \begin{pmatrix} \ddots & \ddots & & & \\ \ddots & \beta_{j-1} & c_{j-1,j} & & \\ & c_{j-1,j} & \beta_j & c_{j,j+1} & \\ & & c_{j,j+1} & \beta_{j+1} & \ddots \\ & & & \ddots & \ddots \end{pmatrix}. \quad (A2)$$

The energy spectrum and corresponding eigenmodes of the coupled waveguide system can be calculated by diagonalizing H.

For the triplet waveguide supercell, the waveguides have identical propagation constant β_0, and the coupling coefficients are c_1 and c_2. The three-level Hamiltonian of the supercell can be written as

$$H = \beta_0 I_{3\times 3} + \begin{pmatrix} 0 & c_1 & 0 \\ c_1 & 0 & c_2 \\ 0 & c_2 & 0 \end{pmatrix}. \quad (A3)$$
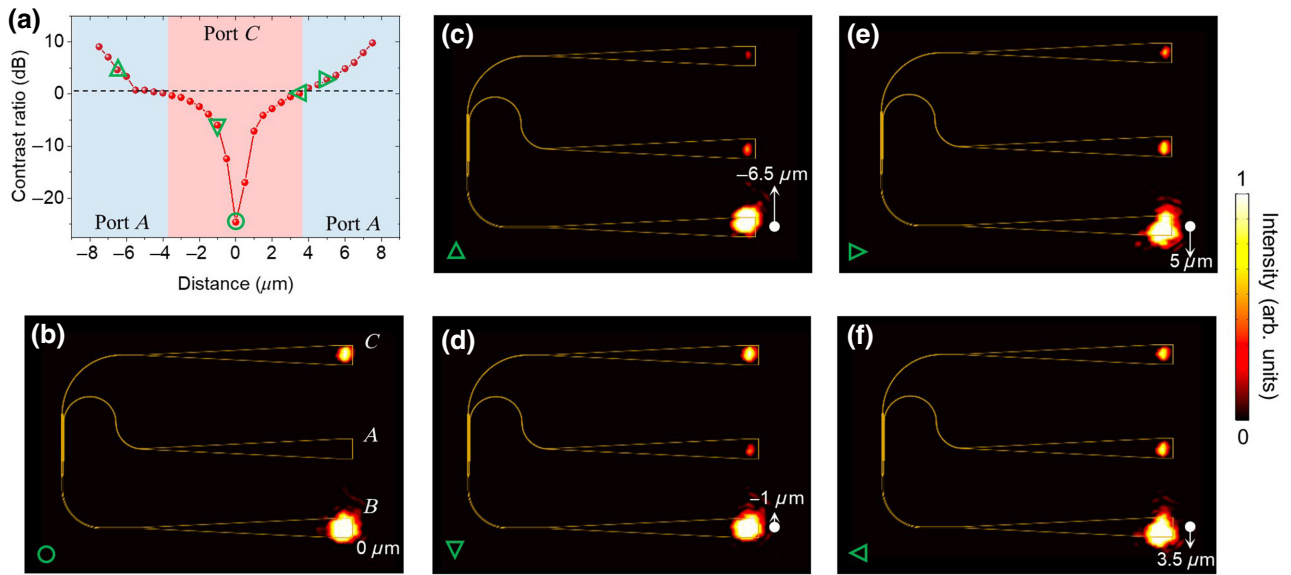

FIG. 6. (a) Experimentally measured extinction ratio for the output intensities of port A and C with different input positions at port B. (b)–(f) Corresponding experimentally captured images.

The energy spectrum and eigenmodes of the supercell are shown in Figs. 1(b) and 1(d) in the main text, where a breathing mode with a zero mode constant and two split translation modes are found. Figure 1(b) is plotted with $c_1 = c_2$.

For the four-waveguide system, the waveguides also have an identical propagation constant β_0, and the triplet waveguide supercell is coupled to a single waveguide with coupling coefficient c' ($c' < c_i$, $i = 1, 2$). In this case, the four-level Hamiltonian can be written as

$$H = \beta_0 I_{4\times4} + \begin{pmatrix} 0 & c_1 & 0 & 0 \\ c_1 & 0 & c_2 & 0 \\ 0 & c_2 & 0 & c' \\ 0 & 0 & c' & 0 \end{pmatrix}. \qquad (A4)$$

The energy spectrum and eigenmodes can also be obtained, as shown in Fig. 1(f) in the main text ($c' = 0.2c_{1(2)}$). Two QZMs form due to the coupling and two split modes remain nearly unchanged.

APPENDIX B: EXPERIMENTAL CONFIRMATION OF THE BREATHING MODE

Figures 5(a) and 5(b) show the schematics and SEM pictures of the fabricated samples with enlarged figures of input and output ports, respectively. Two samples are fabricated with different output waveguides to check the antiphase property of the breathing mode. One sample has two extended waveguides to examine the intensities,
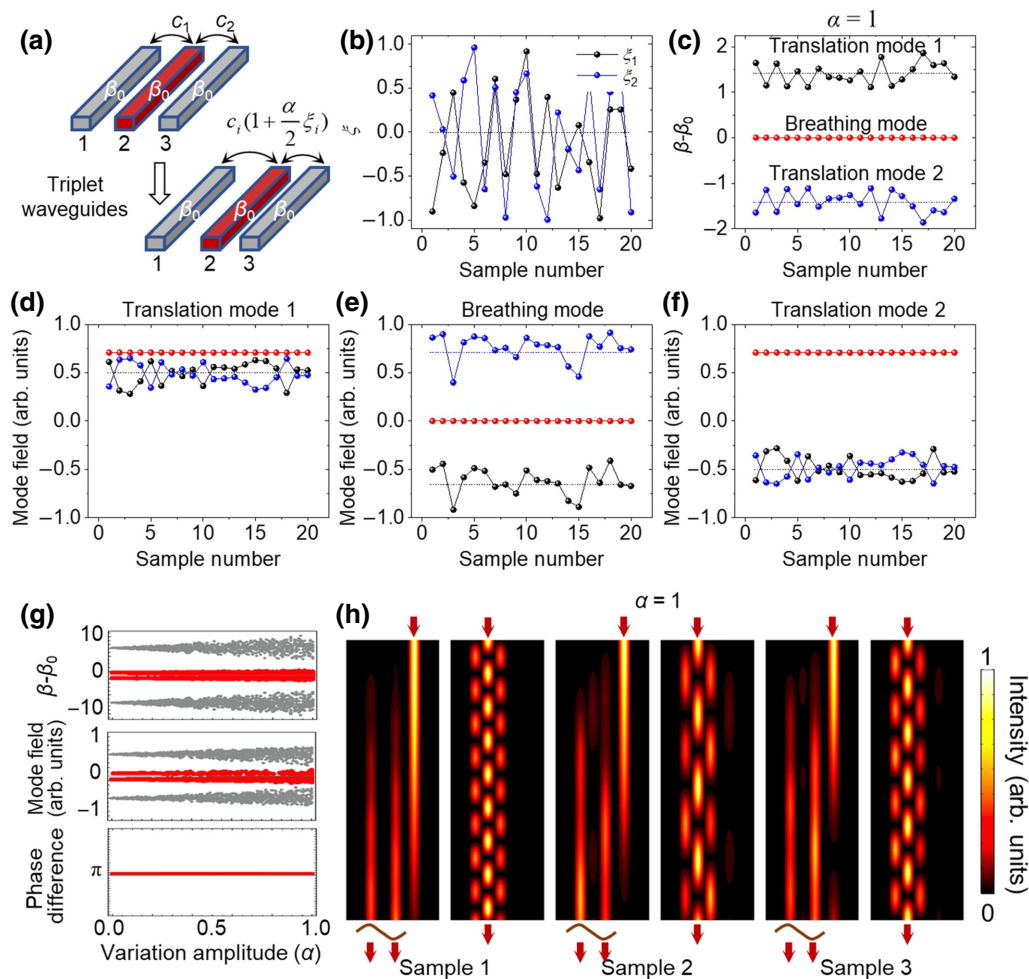

FIG. 7. (a) Applying waveguide position variations to the triplet waveguide supercell, which modifies the coupling coefficient, i.e., $c_i[1 + (\alpha/2)\xi_i]$ ($i = 1, 2$). (b) Randomly generated 20 sets of $\xi_{1,2}$. (c) Mode constants (i.e., eigenvalues of the Hamiltonian of the waveguide supercell) for these samples with waveguide position variations. The dashed lines represent the $c_1 = c_2 = c$ case. It is found that the propagation constant of the breathing mode is not affected by varying coupling strengths. (d)–(f) Corresponding mode amplitude of the waveguide supercell. The breathing mode always has zero field at the center waveguide even with the variations. (g) Mode constants (top), mode amplitude (middle), and output phase difference (bottom) of the four-waveguide system in the presence of position variations, 1000 samples are calculated and presented. It is found that the QZMs are quite stable, showing very small fluctuations under such variations. The exact π-phase difference (antiphased field in waveguide 1 and 3) can also be well preserved at the output. (h) Light-propagation patterns with variations ($\alpha = 1$). Three samples are shown here as examples.

and in the other sample, the two waveguides are combined to examine the phase difference. Figure 5(c) shows the corresponding experimental results of the output port. As expected, two bright spots appear for the sample with two separated waveguides while no light is observed for the other sample with the combined waveguide. It is evident that the devices can generate two outputs with equal intensities and opposite phases, showing the antiphased property of the breathing mode.

APPENDIX C: SAMPLE FABRICATION AND MEASUREMENT

The waveguide arrays and grating nanostructures are fabricated using the method of electron-beam lithography and an inductively coupled plasma-etching process. The substrate we use is 230-nm silicon deposition on 460-μm alumina substrate, the substrates are cleaned in an ultrasound bath in acetone and deionized water for 10 min, respectively, and dried under clean nitrogen flow. Then 400-nm AR-N7520 photoresist film is spin coated onto the substrate and baked at 85 °C for 1 min. After that, the sample is exposed to electron beam in an e-beam writer (Elionix, ELS-F125) and developed to form the AR-N7520 nanostructures. Then, the sample is transferred

into HSE Series Plasma Etcher 200 and etched with C4F8 and SF6 (the flow rates of these two types of gases are 7 5:30 sccm). After the ICP etching, the remaining AR-N7520 is removed by using an O_2 plasma for 5 min.

In optical measurements, a near-infrared (NIR) optical wave at the wavelength of 1550 nm from a single-frequency mode laser (FL-1550-SF) is focused at the input grating via a Mitutoyo 100× long-working distance objective (NA = 0.70, f = 200 mm) from the front side (air). The input power is controlled with a variable neutral-density (ND) filter, and the polarization of input light is tuned through a linear polarizer (LP). The scattered signals from the samples are collected by another 50× NIR objective (NA = 0.42, f = 200 mm) from the backside (substrate), and are imaged by a NIR CCD camera (Xenics Xeva-1.7-320).

APPENDIX D: THE INFLUENCE OF INPUT POSITIONS ON PORT *B*

The extinction of port *A* occurs when the light is focused at the center of the grating of port *B*. If the light spot is off centered, both *A* and *C* will have output signals. Figure 6(a) shows the extinction ratio of the transmitted optical power of port *A* and *C* [$10\log(I_A/I_C)$] as the light spot shifts.
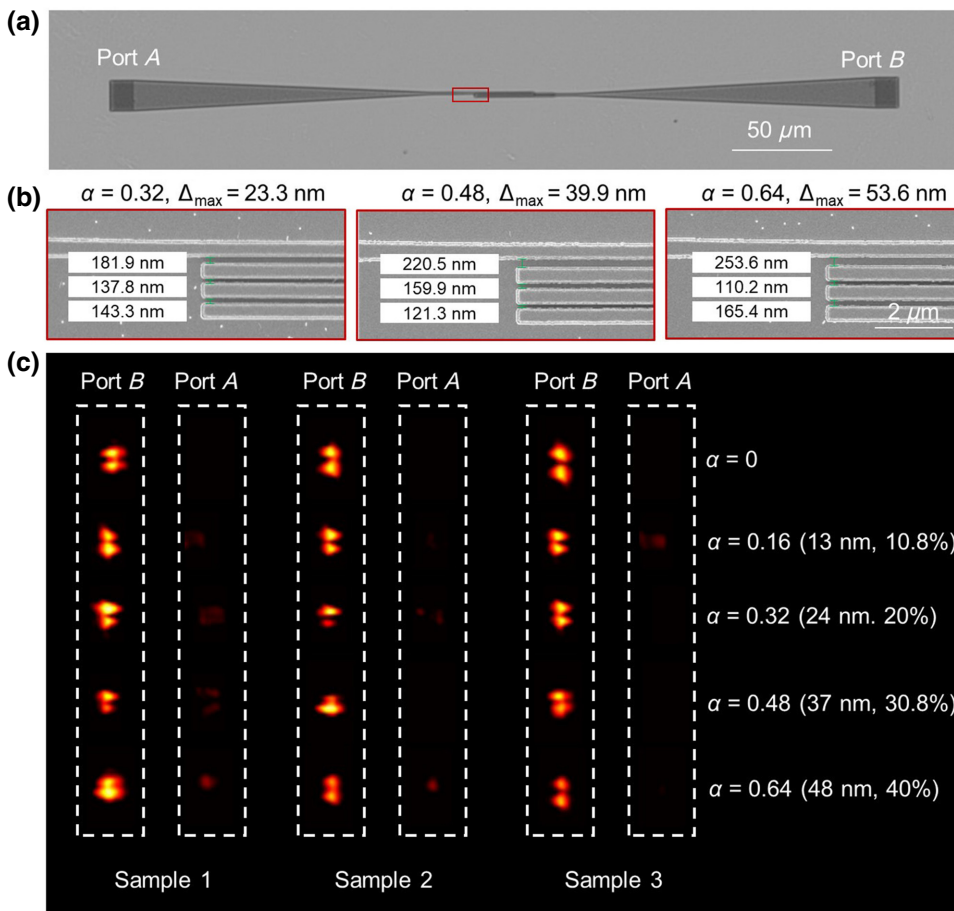

FIG. 8. Microscope image (a) and enlarged SEM images (b) of fabricated samples with random waveguide position variations, where the actual structural parameters (e.g., gap distances) are marked. (c) Corresponding experimental results of port-*A* and -*B* inputs for different α. Three samples are presented as examples for each α.
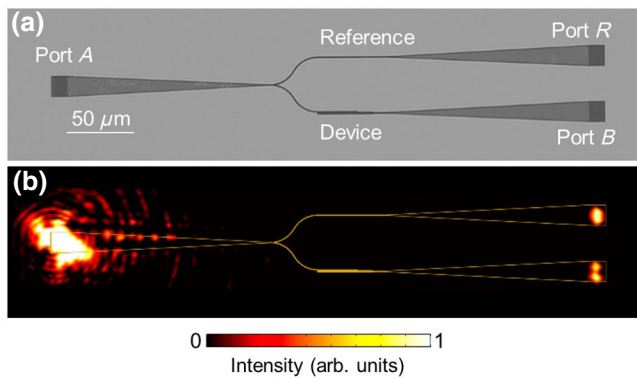
FIG. 9. (a) Microscope image of the fabricated device with the reference straight waveguide. (b) Experimentally detected output scattering fields from port *R* and *B* in the straight waveguide (upper) and our device (bottom).

Figures 6(b)–6(f) show the corresponding experimentally captured images for different spot offset (e.g., 0, −6.5, −1, 5, 3.5 μm). Light indeed comes from port *A* if the input is shifted from the center. We note that the size of the focused laser spot (approximately 10 μm) is smaller than that of the grating (approximately 15 μm). Therefore, the fundamental mode of the multimode waveguide can be excited only when the laser spot is focused at the center of the grating, which leads to the extinction of port *A*. However, if there is an offset of the laser spot, higher-order modes are also excited and routed to port *A* due to the excitation of the QZMs. In this regard, ports *A* and *C* can filter out the translation modes and the QZM signals, respectively.

APPENDIX E: ROBUSTNESS

We verify the robustness of the mode-conversion process both theoretically and experimentally, as shown in Figs. 7 and 8, respectively.

APPENDIX F: INSERTION LOSS

The experimentally captured output scattering fields from port *R* and *B* in straight waveguide (as reference) and the device are shown in Fig. 9, from which we obtain low insertion loss of 0.32 dB for the device (averaged over three samples).

talk, CLEO. Available at https://researcher.watson.ibm.com/researcher/files/us-yvlasov/vlasov_CLEO_Plenary_05092012.pdf (2012).

[5] J. B. Park, D.-M. Yeo, and S.-Y. Shin, Variable optical mode generator in a multimode waveguide, IEEE Photon. Technol. Lett. **18,** 2084 (2006).

[6] Y. Y. Huang, G. Y. Xu, and S.-T. Ho, An ultracompact optical mode order converter, IEEE Photon. Technol. Lett. **18,** 2281 (2006).

[7] V. Liu, D. A. B. Miller, and S. Fan, Ultra-compact photonic crystal waveguide spatial mode converter and its connection to the optical diode effect, Opt. Express **20,** 28388 (2012).

[8] J. Lu and J. Vučković, Nanophotonic computational design, Opt. Express **21,** 13351 (2013).

[9] B. Shen, Ra Polson, and R. Menon, Integrated digital metamaterials enables ultra-compact optical diodes, Opt. Express **23,** 10847 (2015).

[10] S. Molesky, Z. Lin, A. Y. Piggott, W. Jin, J. Vucković, and A. W. Rodriguez, Inverse design in nanophotonics, Nat. Photon. **12,** 659 (2018).

[11] H. Jia, T. Zhou, X. Fu, J. F. Ding, and L. Yang, Inverse-design and demonstration of ultracompact silicon meta-structure mode exchange device, ACS Photonics **5,** 1833 (2018).

[12] D. Ohana, B. Desiatov, N. Mazurski, and U. Levy, Dielectric metasurface as a platform for spatial mode conversion in nanoscale waveguides, Nano Lett. **16,** 7956 (2016).

[13] Z. Li, Z. Li, M.-H. Kim, C. Wang, Z. Han, S. Shrestha, A. C. Overvig, M. Lu, A. Stein, A. M. Agarwal, M. Lončar, and N. Yu, Controlling propagation and coupling of waveguide modes using phase-gradient metasurfaces, Nat. Nanotech. **12,** 675 (2017).

[14] H. W. Wang, Y. Zhang, Y. He, Q. Zhu, L. Sun, and Y. Su, Compact silicon waveguide mode converter employing dielectric metasurface structure, Adv. Opt. Mater. **7,** 1801191 (2019).

[15] J. Guo, C. Ye, C. Liu, M. Zhang, C. Li, J. Li, Y. Shi, and D. Dai, Ultra-compact and ultra-broadband guided-mode exchangers on silicon, Laser Photonics Rev. **14,** 2000058 (2020).

[16] L. Feng, M. Ayache, J. Huang, Y.-L. Xu, M.-H. Lu, Y.-F. Chen, Y. Fainman, and A. Scherer, Nonreciprocal light propagation in a silicon photonic circuit, Science **333,** 729 (2011).

[17] J. Doppler, A. A. Mailybaev, J. Böhm, U. Kuhl, A. Girschik, F. Libisch, T. J. Milburn, P. Rabl, N. Moiseyev, and S. Rotter, Dynamically encircling an exceptional point for asymmetric mode switching, Nature **537,** 76 (2016).

[18] S. N. Ghosh and Y. D. Chong, Exceptional points and asymmetric mode conversion in quasi-guided dual-mode optical waveguides, Sci. Rep. **6,** 19837 (2016).

[19] X.-L. Zhang, T. Jiang, and C. T. Chan, Dynamically encircling an exceptional point in anti-parity-time symmetric systems: Asymmetric mode switching for symmetry-broken modes, Light Sci. Appl. **8,** 88 (2019).

[20] J. W. Yoon, Y. Choi, C. Hahn, G. Kim, S. H. Song, K.-Y. Yang, J. Y. Lee, Y. Kim, C. S. Lee, J. K. Shin, H.-S. Lee, and P. Berini, Time-asymmetric loop around an exceptional point over the full optical communications band, Nature **562,** 86 (2018).

[1] S. E. Miller, Integrated optics: An introduction, Bell Syst. Tech. J. **48,** 2059 (1969).

[2] R. Soref, The past, present, and future of silicon photonics, IEEE J. Sel. Top. Quantum Electron. **12,** 1678 (2006).

[3] B. Jalali and S. Fathpour, Silicon photonics, IEEE J. Light. Technol. **24,** 4600 (2006).

[4] Y. A. Vlasov, Silicon integrated nanophotonics: road from scientific explorations to practical applications. Plenary

[21] A. Li, J. Dong, J. Wang, Z. Cheng, J. S. Ho, D. Zhang, J. Wen, X.-L. Zhang, C. T. Chan, A. Alù, C.-W. Qiu, and L. Chen, Hamiltonian Hopping for Efficient Chiral Mode Switching in Encircling Exceptional Points, Phys. Rev. Lett. **125**, 187403 (2020).

[22] M.-A. Miri, M. Heinrich, R. El-Ganainy, and D. N. Christodoulides, Supersymmetric Optical Structures, Phys. Rev. Lett. **110**, 233902 (2013).

[23] M. Heinrich, M.-A. Miri, S. Stützer, R. El-Ganainy, S. Nolte, A. Szameit, and D. N. Christodoulides, Supersymmetric mode converters, Nat. Commun. **5**, 3698 (2014).

[24] A. Yariv, Coupled-mode theory for guided-wave optics, IEEE J. Quantum Electron. **9**, 919 (1973).

[25] I. L. Garanovich, S. Longhi, A. A. Sukhorukov, and Y. S. Kivshar, Light propagation and localization in modulated photonic lattices and waveguides, Phys. Rep. **518**, 1 (2012).

[26] A. Olivetti, J. Barré, B. Marcos, F. Bouchet, and R. Kaiser, Breathing Mode for Systems of Interacting Particles, Phys. Rev. Lett. **103**, 224301 (2009).

[27] R. Givens, O. F. de A. Bonfim, and R. B. Ormond, Direct observation of normal modes in coupled oscillators, Am. J. Phys. **71**, 87 (2003).